DE GRUYTER OPEN

Chemical and Process Engineering 2017, 38 (1), 51-66

DOI: 10.1515/cpe-2017-0005

PAN

PROCESS DESIGN FOR SIZE-CONTROLLED FLAME SPRAY SYNTHESIS OF $Li_4Ti_5O_{12}$ AND ELECTROCHEMICAL PERFORMANCE

Oliver Waser[1], Oliver Brenner[1], Arto J. Groehn[2], Sotiris E. Pratsinis[*1]

[1]Particle Technology Laboratory, Department of Mechanical and Process Engineering, ETH Zurich, Sonneggstrasse 3, CH-8092 Zurich, Switzerland

[2]Department of Chemical and Biological Engineering, University of Colorado, Boulder, 80309 CO, USA

Dedicated to Prof. Leon Gradoń on the occasion of his 70th birthday

Inexpensive synthesis of electroceramic materials is required for efficient energy storage. Here the design of a scalable process, flame spray pyrolysis (FSP), for synthesis of size-controlled nanomaterials is investigated focusing on understanding the role of air entrainment (*AE*) during their aerosol synthesis with emphasis on battery materials. The *AE* into the enclosed FSP reactor is analysed quantitatively by computational fluid dynamics (CFD) and calculated temperatures are verified by Fourier transform infrared spectroscopy (FTIR). Various $Li_4Ti_5O_{12}$ (LTO) particle compositions are made and characterized by N_2 adsorption, electron microscopy and X-ray diffraction while the electrochemical performance of LTO is tested at various charging rates. Increasing *AE* decreases recirculation in the enclosing tube leading to lower reactor temperatures and particle concentrations by air dilution as well as shorter and narrower residence time distributions. As a result, particle growth by coagulation – coalescence decreases leading to smaller primary particles that are mostly pure LTO exhibiting high C-rate performance with more than 120 mAh/g galvanostatic specific charge at 40C, outperforming commercial LTO. The effect of *AE* on FSP-made particle characteristics is demonstrated also in combustion synthesis of $LiFePO_4$ and ZrO_2.

Keywords: Li-ion battery, $Li_4Ti_5O_{12}$, size control, residence time distribution, computational fluid dynamics, flame synthesis of electroceramics

1. INTRODUCTION

With the spread of electric-mobility and renewable energy applications the need for inexpensive, safe and long-lasting energy-storage systems arises (Poullikkas, 2013). Batteries are well suited for this task (Armand and Tarascon, 2008) with the inherently safe LTO anode (Ferg et al., 1994) and LFP cathode materials (Padhi et al., 1997). Both are promising due to their low cost, abundant raw materials and environmental friendliness as well as performance in Li-ion batteries and novel hybrid supercapacitors made of LTO (Naoi et al., 2013) or LFP (Vlad et al., 2014). Furthermore, the negligible volume change of LTO during charging – discharging, zero-strain insertion (Ohzuku et al., 1995), results in outstanding cycle stability (Du Pasquier et al., 2009). Furthermore, LTO anode electrodes can be built with about three times lighter aluminium current collectors compared to the typically required Cu since the LTO insertion potential vs. Li/Li^+ is relatively high (> 1.2 V) and Li alloying of aluminium can be excluded (Hudak and Huber, 2012). A challenge of both materials, however, is their poor Li diffusion,

*Corresponding author, e-mail: sotiris.pratsinis@ptl.mavt.ethz.ch

10^{-12} cm^2/s for LTO (Wagemaker et al., 2009) and less than 10^{-9} cm^2/s for LFP (Gaberscek et al., 2007), hindering Li-ion transport during fast charge - discharge. Nanosizing LFP (Gaberscek et al., 2007) and LTO (Bresser et al., 2012), however, has shown distinct performance improvement by shortening the diffusion path lengths.

To take advantage of nanosize, economic synthesis methods are needed to preserve the benefit of low cost raw materials for LTO and LFP. Flame aerosol reactors have high potential in that front since they already produce several tons per hour of nanostructured carbon blacks for tire reinforcing and inks, TiO_2 for white pigments and catalysis or fumed SiO_2 as flowing aid and excipient for drugs (Pratsinis, 1998, Wegner and Pratsinis, 2003). These, typically gas-fed, flame aerosol reactors have limited precursor selection where the liquid-fed flame spray pyrolysis (FSP) (Madler et al., 2002) offers wide precursor flexibility (Teoh et al., 2010) for multi-component nanoparticles and close control over particle size and phase resulting in an array of functional materials (Strobel and Pratsinis, 2007).

More specifically, FSP has been applied for synthesis of nanosized battery active $LiMn_2O_4$, LTO and $LiFe_5O_8$ (Ernst et al., 2007) as well as LFP after annealing of amorphous precursor nanoparticles under reducing conditions (Waser et al., 2011) and very high charging rate (C-rate) capable LTO nanoparticles (Bresser et al., 2012). This FSP process is scalable (Mueller et al., 2003) to, at least, 10 metric tons per year production rate (Wegner et al., 2011) as it is similar to the furnace process for manufacture of carbon blacks (Strobel and Pratsinis, 2007). For such scale-up, however, process design by computational fluid dynamics (CFD) (Johannessen et al., 2000) is essential for understanding the effect of process variables to product particle characteristics as with FSP production of ZrO_2 (Groehn et al., 2012, Groehn et al., 2014).

Tube-enclosed FSP (Teleki et al., 2006) allows better control of the combustion environment to produce, for example, metallic nanoparticles (Athanassiou et al., 2006), select the product composition between maghemite, magnetite or wustite iron oxides (Strobel and Pratsinis, 2009), or anatase and rutile TiO_2 (Kho et al., 2011). Tube enclosing also allows in-situ SiO_2 coating on TiO_2 (Teleki et al., 2008), or Ag (Sotiriou et al., 2010) and carbon-coating of LFP nanoparticles (Waser et al., 2011). Recent in-situ XRD & microscopy (Krumeich et al., 2016) has shown that crystallization of the initially glassy carbon-coated LFP starts at about 400 °C, forming single crystals inside the confinement of the carbon shell. At about 700 °C, LFP starts to diffuse through the carbon shell creating cavities inside the shell. At 800 °C, the initial core-shell morphology converts into open carbon shells (flakes and cenospheres) and rather bulky LFP particles (300–400 nm in diameter) (Krumeich et al., 2016), in agreement with ex-situ experiments (Waser et al., 2011).

Particles made by enclosed FSP are typically 3-4 times larger than those made by open FSP under identical reactant flows and compositions as has been shown with TiO_2 and iron oxides above as well as CuO (Waser et al., 2013). Particle size control in tube-enclosed FSP can be accomplished also quite inexpensively by selectively allowing ambient air entrainment into the FSP unit as has been shown recently for CuO (Waser et al., 2014).

Here we generalize this method for primary particle size control during synthesis of nanosized battery active LTO and amorphous LFP precursor as well as ZrO_2 by tube-enclosed FSP. The spatial distributions of temperature and residence time in the reactor are elucidated by CFD and the particle size dependent electrochemical performance of LTO is evaluated in Li-ion test cells.

2. EXPERIMENTAL

2.1. Particle Synthesis

Nano-sized LTO, amorphous LFP precursor and ZrO_2 particles were made by FSP of precursor solutions in open (Madler et al., 2002) and tube-enclosed configurations (Waser et al., 2014). For the latter, a 20-cm long quartz glass tube of 4.7 cm inner diameter (ID) and 0.25 cm wall thickness was used. The (forced) air entrainment into this tube was controlled by a mass flow controller (MFC, Bronkhorst, Netherlands) through a stainless steel drum of 15 cm ID and 8 cm inner height surrounding the 1.0 cm gap between the FSP burner surface and the enclosing tube (Waser et al., 2014).

The LTO precursor solution (1.0 M total metal concentration) consisted of Li-acetylacetonate (Li-acac 97 %, Sigma-Aldrich, Switzerland) and Ti(IV)-isopropoxide (TTIP ≥ 97 %, Sigma-Aldrich, Switzerland) in stoichiometric molar ratio of Li / Ti = 4 / 5, diluted with a 1 / 3 (by volume) mixture of 2-ethylhexanoic acid (2-EHA, Sigma-Aldrich, Switzerland) and xylene (Sigma-Aldrich, Switzerland) solvents. For the FTIR temperature measurements and CFD calculations a metal-free solvent mixture was used where the TTIP is equivolumetrically replaced by isopropyl alcohol (2-propanol ≥ 99.5 %, Sigma-Aldrich, Switzerland) resulting in a volume-ratio of 1 / 3 / 0.787 of 2-EHA / xylene / 2-propanol and thus in approximately the same enthalpy density of 33 MJ/L (< 1 % deviation) as the above metal-containing precursor solution.

Similarly, the LFP precursor solution (0.24 M total metal concentration) consisted of Li-acetylacetonate (Li-acac ≥ 97 %, Sigma-Aldrich, Switzerland), iron (III) - acetylacetonate (Fe-acac ≥ 99%, Fluka, Switzerland) and tributyl phosphate (≥99 %, Fluka, Switzerland) in stoichiometric molar ratio of Li / Fe / P = 1 / 1 /1, diluted with an equivolumetric mixture of 2-EHA, toluene (Sigma-Aldrich, Switzerland), diethylene glycol monobutyl ether (purum ≥ 98%, Fluka, Switzerland) and ethanol (98 %, Alcosuisse, Switzerland) (Waser et al., 2011). The ZrO_2 precursor solution (1.0 M Zr concentration) consisted of zirconium 2-ethylhexanoate (Valirex, 18 wt % Zr, Umicore) in xylene (Sigma-Aldrich, Switzerland) (Groehn et al., 2014). These solutions were fed to the FSP burner capillary at P = 5 mL/min and dispersed into a spray by D = 5 L/min O_2 (PanGas > 99.95 %) at 180 kPa (gauge) pressure drop resulting in nominal LTO, LFP and ZrO_2 production rates of 15.3, 3.9 and 37 g/h, respectively. The spray was ignited and supported by a stoichiometrically premixed pilot flame of 1.25 L/min CH_4 (PanGas > 99.5 %) and 2.5 L/min O_2 surrounding the dispersion O_2 annulus. In all experiments S = 10 L/min of sheath O_2 was introduced through 32 holes (0.06 cm *ID*) surrounding the pilot flame to ensure full oxidation of the precursor (Rudin et al., 2011). All gas flow rates are given at STP. The product particles were collected on glass-fibre filters (ALBET GF6, 25.7 cm in diameter) by a vacuum pump (Busch Mink MM 1324AV).

2.2. CFD Simulations

Commercial ANSYS Fluent v.12.1.4 was used on a two-dimensional (rotation symmetric) rectangular computational grid (height 35 cm, width 10 cm, approx. 10^5 cells) based on Groehn et al. (2012) with the difference of having a tube enclosure and adapted solvent mixture composition (without metal precursors) and flows to simulate synthesis of LTO. Radiation heat transfer was accounted for by the Fluent's built-in discrete ordinate model complemented with a weighted-sum-of-gray-gases model and user-specified gas mean beam length L^0 = 4.3 cm (Olfe, 1961). Furthermore, the dissociation energy of CH_4, CO_2, N_2, H_2O and O_2 was accounted for and a transition shear stress transport turbulence model was used instead of the classic k-ε since laminar flow patterns are present within the tube.

The residence time distributions were simulated by introducing a 10 ms pulse of 2 L/min Ne tracer along with 8 L/min O_2 sheath (to maintain the total of 10 L/min sheath gas flow). The pulse response was evaluated 0.5 cm above the tube exit (Octave, 1999). This was done after convergence of the actual (steady state) simulations by a separate transient simulation (Gamba et al., 2012) of the Ne concentration (Waser et al., 2014) by solving only the Ne transport equation with a time step size of 10^{-4} s. For details about the CFD boundary conditions please refer to Table A1 and Fig. A1 of the Appendix.

2.3. Temperature measurements

The line-of-sight tube exit temperature of the FSP gases during LTO synthesis was measured 0.5 cm above the tube exit by Fourier transform infrared spectroscopy (FTIR) by emission / transmission analysis (Morrison et al., 1997). Thereby, a metal precursor-free solvent mixture (2-EHA / xylene / 2-propanol = 1 / 3 / 0.787) was combusted with P = 5 ml/min and D = 10 L/min O_2, accompanied by S = 10 L/min O_2 sheath. The shaded area (Fig. 2) represents the difference between FTIR emission / transmission and normrad analysis spectra (Madler et al., 2002) while the solid red line is their average.

2.4. Particle and electrochemical characterization

Product powders were characterized by X-ray diffraction (XRD) for crystallinity (Bruker D8, Germany) and N_2 adsorption (5-point isotherm) for specific surface area, SSA (Micromeritics, Tristar 30000). The Brunauer–Emmett–Teller (BET) diameter is used as the average primary particle diameter, $d_{BET} = 6 / (SSA \times \rho)$, with bulk densities ρ of LTO: 3.48 (Deschanvres et al., 1971), LFP: 3.60 (Streltsov et al., 1993), CuO: 6.52 (Asbrink and Norrby, 1970) and ZrO_2: 5.72 g/cm^3 (Whitney, 1994), respectively.

The electrochemical performance of the LTO particles is evaluated in Li-ion battery half-cells vs. Li/Li^+. As-prepared LTO nanoparticles from open and enclosed FSP with AE = 50, 100, 200 and 300 L/min, respectively, are used as active material (AM). Carbon black (CB; Super P, TIMCAL SA, SSA = 62 m^2/g) was used as a conductive additive. Polyvinylidene fluoride (PVDF; SOLEF 5130, Solvay) dissolved in N-methylpyrrolidinone (NMP; Fluka) was used as binder. Since electrode mass loading and CB content strongly influence the high C-rate performance of Li-ion electrodes (Zheng et al., 2012) two sets of electrodes were made to benchmark the LTO performance. One set of electrodes was made with an electrode mass-ratio (after drying) of AM / CB / PVDF of 80 / 10 / 10 (Nowack et al., 2013) and a second one with 70 / 15 / 15 (Bresser et al., 2012). The suspensions were prepared by mixing all constituents in NMP with an ultrasonic stirrer (Vibra-Cell VCX 500, Sonics, USA) for about 2 min at 100 W and 20 kHz using a micro-tip.

To prepare test electrodes, suspensions were doctor-bladed at a ‘‘wet’’ thickness of 250 μm (80 / 10 / 10 composition) and 150 μm (70 / 15 / 15 composition) onto a 20 μm thick conductive carbon-coated aluminium current collector foil (EQ-CC-Al-20u-260, MTI, USA) and dried at 110 °C under vacuum overnight. Afterwards, disk electrodes of diameter 1.3 cm were punched out and dried again under vacuum at 110 °C overnight. The AM mass loading was 2.8 ± 0.1 mg/cm^2 for the 80 / 10 / 10 composition and 1.5 ± 0.15 mg/cm^2 for the 70 / 15 / 15 composition of the FSP-made LTO. The AM mass loading of commercial LTO was 2.0 ± 0.3 mg/cm^2 for both compositions. Coin-type test cells were assembled in an argon-filled glove box with less than 1 ppm of O_2, N_2, and H_2O. Lithium metal (99.9 %, Aldrich) served as both reference and counter electrode. A fiberglass separator (1 mm thick) was soaked with 500 μl of standard electrolyte 1 M LiPF6 in ethylene carbonate (EC) / dimethyl carbonate (DMC), 1:1 by mass (Selectilyte LP 30, BASF, Germany).

All electrochemical measurements (MPG-2, Bio-Logic, France) were performed at 25 °C and specific current corresponding to 0.1 – 50 C (1 C = 175 mA/g of LTO). For the rate capability measurements, the LTO electrodes were galvanostatically lithiated at the specified C-rate and delithiated at 1 C between 1.2 and 2.2 V vs. Li/Li^+. To promote complete lithiation / delithiation at the respective potential limits, a potentiostatic step was included until the specific current decreased to 17.5 mA/g (0.1 C). All electrochemical results are the average of three cells and error bars show the standard deviation.

3. RESULTS AND DISCUSSION

3.1. Temperature Distribution and Flow Streamlines

Figure 1 depicts the temperature distribution by CFD above the FSP burner as a function of air entrainment (*AE*) flow rate into the tube enclosure (from a to e) in comparison to open FSP (g) with overlaid streamlines. At low *AE* (< 100 L/min), a recirculation zone forms that is typical for bounded jets with limited co-flow (Curtet, 1958). The recirculation mass flow, m_r (fluid flow with negative velocity), relative to the net mass flow, m_0, (f) is shown as a function of height above the burner (HAB). Increasing the *AE* reduces the m_r / m_0 to practically zero for *AE* ≥ 100 L/min (Fig. 1f).

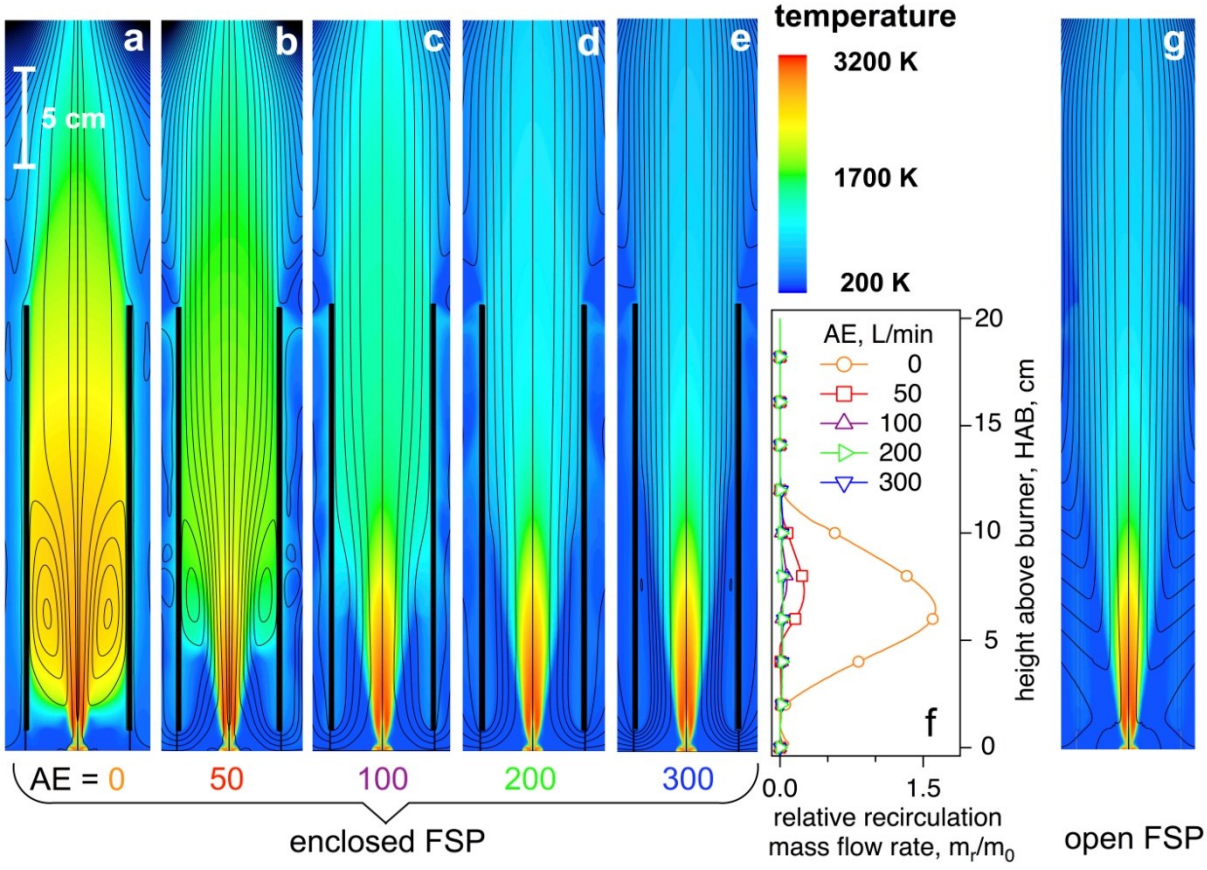

Fig. 1. Temperatures and flow streamlines by computational fluid dynamics (CFD) at air entrainment flow rate *AE* = 0, 50, 100, 200, 300 L/min into the enclosing tube for flame spray pyrolysis (FSP) of a solvent mixture (a to e), simulating $Li_4Ti_5O_{12}$ production, in comparison to open FSP (g). The relative recirculation mass flow (m_r/m_0) as a function of height above burner (f) is defined as the backflow (m_r) relative to the net mass flow (m_0) in the tube cross section and shows that up to about 150 % the net mass flow recirculates in the lower half of the tube (circles) in the absence of air entrainment (*AE* = 0 L/min). This recirculation decreases markedly with increasing *AE* to about 20 wt% of the net mass flow rate at *AE* = 50 L/min and practically ceases at *AE*≥ 100 L/min

Figure 1 illustrates also that the overall temperature within the tube decreases with increasing *AE* due to dilution, in agreement with such measurements at the tube exit for CuO synthesis (Waser et al., 2014). In the absence of entrained air (*AE* = 0 L/min, Fig 1a), the recirculation vortex and the extended high temperature zone in the reactor impose prolonged particle residence time at high temperature that typically leads to extended particle growth. In contrast, for increasing *AE* (50 – 100 L/min), that vortex shrinks and the overall temperature in the tube drops reducing particle growth. For *AE* ≥ 200 L/min, the temperature distribution and flow pattern are similar to those of the open FSP (Fig. 1g), consistent with similar product particle primary diameters from both FSP configurations for CuO (Waser et al., 2014) and as will be shown in Fig. 4.

Figure 2 shows the measured (circles) and CFD-calculated (diamonds) line-of-sight averaged temperature at the tube exit as a function of *AE*. The emission / transmission and normrad analyses of the FTIR spectra only deviate (shaded area in Fig. 2) at the completely enclosed configuration (*AE* = 0 L/min) due to strong IR absorption of CO_2 in such un-diluted off-gas. The aerosol temperature at 21.5 cm HAB of the open FSP configuration is shown to the right of Fig. 2. This HAB corresponds to the tube exit temperature above the enclosed FSP (1 cm tube lift-off from the FSP burner plus 20 cm tube length and 0.5 cm distance above the tube). As expected, the tube exit temperature decreases with increasing *AE* due to air dilution and cooling in agreement with temperature measurements during CuO synthesis by FSP (Waser et al., 2014).

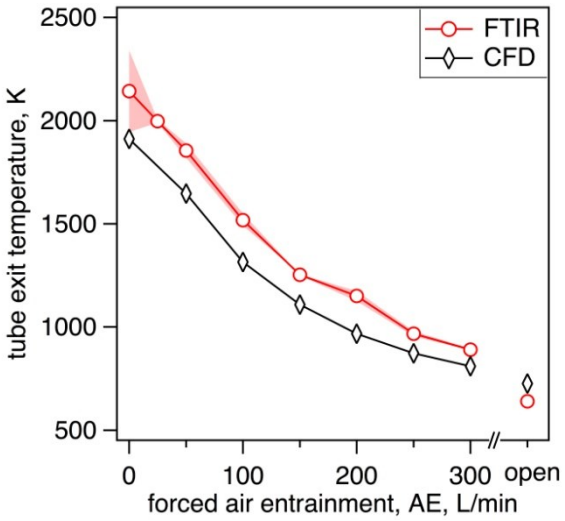

Fig. 2. Tube exit temperature at 0.5 cm height above the enclosing tube (HAT) exit during combustion of solvent mixture simulating LTO production by FTIR (red circles) and line-of sight averaged CFD temperature profile (black diamonds). As comparison, the temperatures for open FSP at 21.5cm (1 cm gap + 20 cm tube + 0.5 cm HAT) above FSP burner level are displayed to the right.

3.2. Aerosol Residence Time Distribution

Reasonably good agreement is obtained between temperature measurements and CFD simulations, however, with a consistent underprediction of about 50 - 200 K by CFD. This might be due to the rather simple eddy dissipation model (Magnussen and Hjertager, 1977) employed by CFD or the relatively simple discrete ordinate radiation model and assumptions for the gas radiative properties (Olfe, 1961). No significant differences in the FTIR spectra of effluent gases at various AE flow rates were observed indicating that chemical reactions had been completed at the tube exit regardless of AE flow rate (Mueller et al., 2004).

At low *AE* flow rates (< 100 L/min, Fig.1), vortices are formed that greatly influence the aerosol residence time distribution (RTD) within the tube und thus the time available for particle growth.

Figure 3a depicts such CFD calculated RTD's for various *AE* flow rates. The mean residence time, τ (triangles) and geometric standard deviation, σ_g, (diamonds) of these RTDs are presented in Fig. 3b. For no *AE* (0 L/min), strong recirculation is present (Fig. 1) resulting in the longest and broadest RTD (Fig. 3a, solid line) compared to higher *AE* of 50 – 300 L/min. Increasing the *AE* to 50 L/min reduces the mean residence time, τ, (Fig. 3b, triangles) by a factor of 3.5 from about 300 to 90 ms where further increasing the AE from 50 to 300 L/min gradually decreases τ to 40 ms. The spread of the RTD, given by σ_g (Fig. 3b, diamonds), shows also a distinct narrowing from $\sigma_g = 2.1$ at $AE = 0$ to $\sigma_g = 1.4$ at $AE = 50$ L/min in agreement with the disappearance of the recirculation zone (Fig.1). Upon further increasing the AE, the spread of the RTD remains largely invariant around $\sigma_g = 1.5$. So, increasing the *AE* clearly reduces the average high temperature residence time as both τ and *T* (Fig. 2) decrease by air dilution along with the precursor concentration. In combination, this results in smaller primary particles as shown for CuO (Waser et al., 2014).

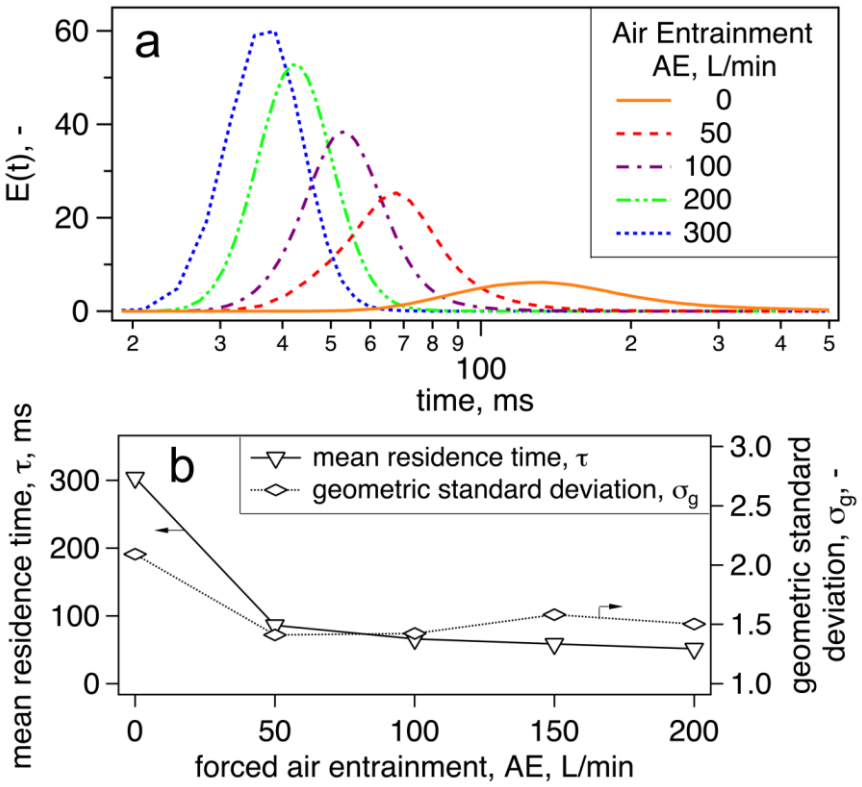

Fig. 3. (a) CFD-calculated aerosol residence time distributions within the enclosing tube at various airentrainment (*AE*) flow rates. At $AE = 0$ the RTD is longest and exceptionally wide, typical for recirculating flows (Fig.5.1) resulting in high particle deposition on tube walls. (b) Mean residence time (τ, triangles) & geometric standard deviation (σ_g, diamonds). The, τ decreases with increasing *AE* due to higher volume flow and reduced recirculation that narrow σ_g

Figure 4 presents the average primary particle diameter (d_{BET}) as a function of *AE* flow rate into the enclosed FSP unit for synthesis of LTO (open squares), LFP (diamonds) and ZrO_2 (circles) in comparison to CuO (triangles (Waser et al., 2014)) as well as the average LTO crystallite size (filled squares) by XRD (Fig. 5). The particle sizes from open FSP are shown to the right while selected images of LTO (a-c), ZrO_2 (d, e) and CuO (f) are presented as insets. Clearly, the largest primary particles are obtained at $AE = 0$ L/min for all materials as expected from their longest residence time (Fig. 3b) and highest aerosol concentration and temperature (Figs. 1 and 2) in the tube. For increasing *AE*, the d_{BET} of LTO, LFP and ZrO_2 decrease consistent with CuO (Waser et al., 2014) shown here also for convenience.

The individual materials, however, show a different d_{BET} evolution as a function of *AE* that depends on precursor solution concentration (Table 1) and material properties. High *AE* rapidly quenches the hot aerosol resulting in short high temperature residence time (Fig. 1e,g) similar to open FSP (Madler et al., 2002). In contrast, at low *AE* the high temperature region is greatly increased (Fig. 1a,b) and shows a smoother temperature decay compared to open FSP or high-*AE* enclosed FSP (Figs. 1a,b vs. 1e,g). So, decreasing the *AE* prolongs the residence time for primary particle growth by sintering or coalescence. This generally favours low-melting-point compounds (Table 1) to grow larger than high-melting-point ones. Furthermore, particle morphology depends on the interplay of sintering and collision rate: Monolithic particles are formed if sintering is faster than collision rate and aggregates if collision is faster than sintering rate (Pratsinis, 1998). So, at *AE* = 0 L/min (Fig. 4), the average LTO primary particles grow to rather spherical and non-aggregated ones having the largest d_{BET} = 63 nm (squares) as seen by microscopy (Fig. 4a). This indicates collision-limited growth of the comparatively low melting point LTO (m_p = 1290 K, Table 1).

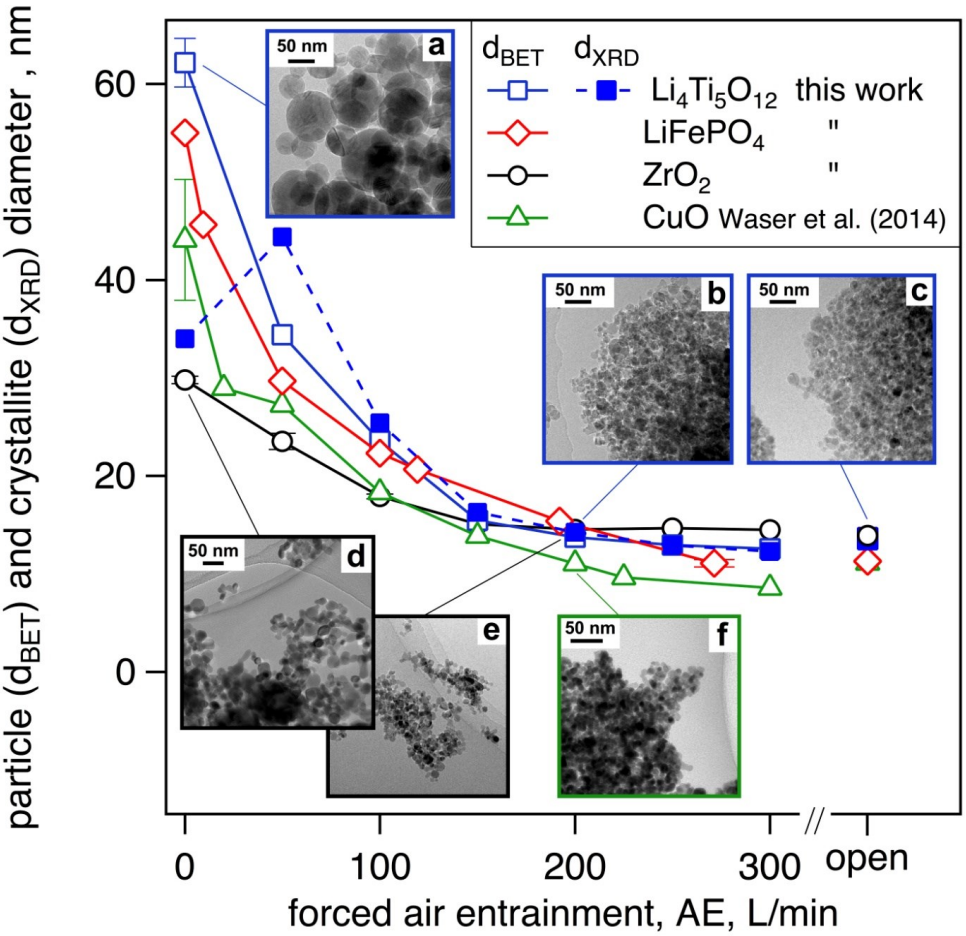

Fig. 4. Primary particle (d_{BET}, open symbols) and LTO crystallite diameter (filled squares) as a function of *AE* of LTO (squares) and LFP (diamonds), ZrO_2 (circles) and CuO (triangles, Waser et al. 2014) made by tube-enclosed FSP. As comparison, the d_{BET} from open FSP are displayed to the right. Insets show selected TEM images of LTO made at *AE* of (a) 0, (b) 200 L/min and (c) open FSP, ZrO_2 made at *AE* of (d) 0 and (e) 200 L/min as well as CuO made at *AE* of (f) 200 L/min

The LTO is further analysed by XRD and electrochemistry, as it is highly crystalline as-prepared. Figure 5 shows the XRD patterns (inset) of LTO made in open and tube-enclosed FSP at *AE* from 0 to 300 L/min along with the corresponding phase composition in terms of LTO (squares, ICSD 015787) and impurities: $Li_{0.14}TiO_2$ (stars, ICSD 075178), anatase (circles, ICSD 063711) and rutile TiO_2 (triangles, ICSD 080843). For *AE* = 0 L/min (orange pattern), the particles have a high impurity content of about 38 wt% $Li_{0.14}TiO_2$, 30 wt% rutile and 3 wt% anatase TiO_2 but only 29 wt% of the desired

LTO. This indicates suboptimal synthesis conditions with reactor temperatures (Fig. 2) approximately twice as high as usually applied for LTO production via solid-state reaction (Ferg et al., 1994), accompanied also by wide particle size distributions and poor yield due to long and broad RTD and deposition wall losses. For $AE \geq 50$ L/min, however, more than 95 wt% pure LTO is obtained with only minor impurities of anatase and rutile TiO_2. This appears superior to as-prepared LTO by open FSP (Ernst et al., 2007) with 87 wt% LTO content and d_{BET} of 20 nm and FSP-made nano LTO by Bresser et al. (2012) but similar to that by Karhunen et al. (2011).

Table 1. Precursor solution molarity & enthalpy with nominal production rate & melting temperature

Material	Metal concentration, mol/L	Combustion enthalpy, MJ/L	Production rate, g/h	Bulk melting temperature, K
LTO	1	33.1	15.3	1290
LFP	0.24	30.3	3.9	1320
CuO	0.25	31.8	6.0	1510
ZrO_2	1	33.6	37.0	2990

The LTO crystallite size d_{XRD} = 34 nm (Fig. 4, filled squares), determined from the peak with the Miller indices hkl = 111, at AE = 0 L/min is significantly smaller than its d_{BET} = 62 nm, as expected by its large impurity content (Birozzi et al., 2015). For AE = 50 L/min, however, the LTO average crystallite size (d_{XRD} = 44 nm) is larger than the average grain size (d_{BET} = 34 nm). This might indicate a rather broad LTO particle size distribution as shown by Rudin et al. (2011) for B_2O_3 nanoparticles and can occur by recirculation within the tube enclosure (Fig. 1b,f). For AE > 50 L/min the LTO crystallite size then continuously decreases from d_{XRD} = 26 to 14 nm, practically overlapping with d_{BET}. This indicates monocrystalline LTO.

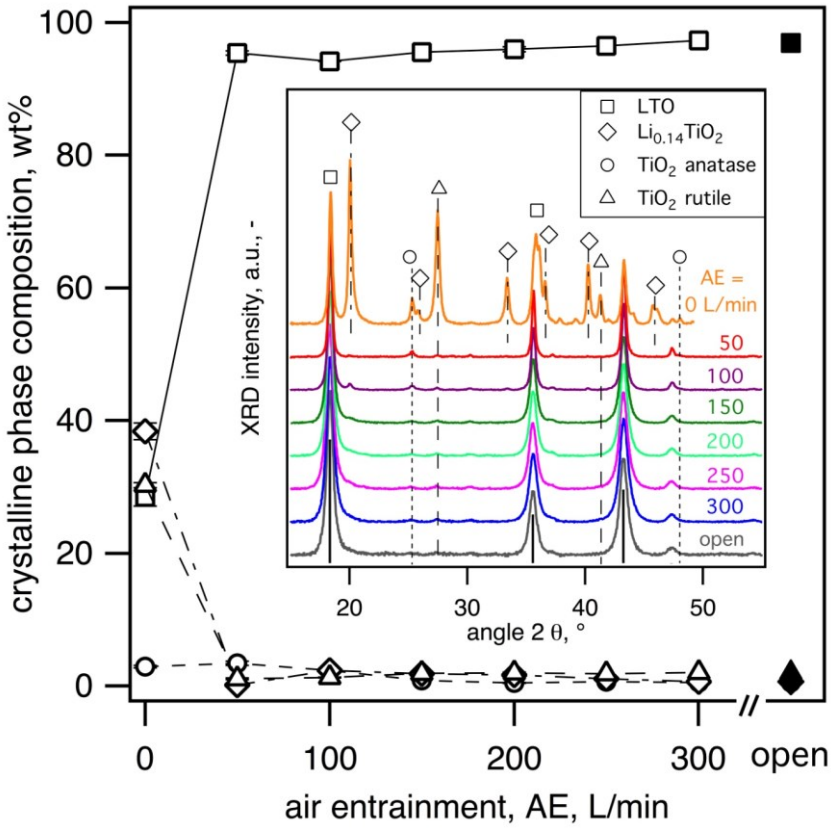

Fig. 5. XRD phase composition and patterns (inset) of as-prepared LTO particles made in tube-enclosed-FSP (open symbols) as a function of air entrainment (AE) in comparison to particles made in open- FSP (filled symbols)

It should be noted that the d_{BET} is larger than d_{XRD}. This is an intrinsic effect of the applied measurement techniques of d_{BET} (surface area derived particle diameter) and d_{XRD} (crystallite size derived particle diameter). So, if a particle contains a crystallite of LTO surrounded by other crystalline impurity or even amorphous phases the d_{BET} measures the whole particle and thus becomes larger than the d_{XRD}. The XRD, however, measures the core LTO crystallite diameter only.

3.3. Electrochemical performance

Figure 6 shows the specific charge of the thicker (2.8 mg/cm^2) electrodes upon the first lithiation (solid line) and the following delithiation (dotted line) of as-prepared LTO with average primary particle sizes of d_{BET} = 13, 14, 23 and 34 nm corresponding to those made at *AE* of 300, 200, 100 and 50 L/min (Fig. 4 squares). The theoretical specific charge of $Li_{4+x}Ti_5O_{12}$ ($0 < x \leq 3$) is depicted as horizontal dashed line. The initial specific charge for the smallest LTO particles of d_{BET} = 13 and 14 nm is higher than the theoretical limit of 175 mAh/g (Ohzuku et al., 1995). It seems also to scale with increasing particle surface area exposed to the electrolyte since larger FSP-made (d_{BET} = 23 and 35 nm) and commercial LTO (d_{BET} = 177 nm) show specific charges below the theoretical limit.

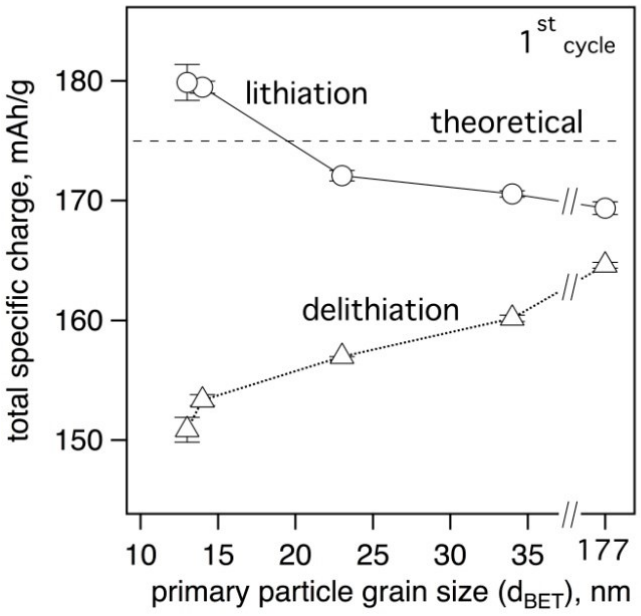

Fig. 6. Total specific charge upon first lithiation (solid line, circle) and following delithiation (dotted line, triangles) of electrodes made with as-prepared LTO nanoparticles as a function of primary particle size. The performance of commercial LTO (d_{BET}= 177 nm) is shown to the right for comparison. The horizontal dashed line indicates the LTO's theoretical specific charge of 175 mAh/g. The specific charge upon initial lithiation inversely scales with primary particle size due to irreversible surface reactions with the electrolyte. This results in higher lithiation specific charges than theoretically expected for the smallest LTO particles of d_{BET}=13 and 14 nm while the delithiation charges remain below the theoretical limit

A similar effect was observed for nanosized, FSP-made CuO particles used as conversion reaction battery material (Waser et al., 2013) where solid-electrolyte-interface (SEI) formation consumed Li (Laruelle et al., 2002). Here the extra specific charge might also be attributed to the formation of LiF, Li_2CO_3 and TiO_2 on the lithiated particle surfaces (Jiang et al., 2004). A more recent study shows approximately 3 nm thick surface layers containing anatase phase TiO_2 after immersion of the originally pure LTO particles in electrolyte solution (He et al., 2012). These reactions seem irreversible since the specific charge upon the following delithiation remains below the theoretical limit of

175 mAh/g, regardless of primary particle diameter. The trend of low specific charge upon delithiation of small LTO particles may be attributed to more pronounced LTO lattice defects in small particles (Kavan et al., 2003) resulting in lower specific charge. This results in 1st cycle coulombic efficiencies of 84, 85, 91, 94, and 97 % for d_{BET} = 13, 14, 23, 34, and commercial 177 nm LTO particles, respectively. This is in good agreement with FSP-made nano LTO (Bresser et al., 2012) also having lower columbic efficiencies of about 77 % for nanosized LTO (d_{BET} = 19 nm) compared to 94 % for micron sized particles.

Figure 7 depicts the galvanostatic specific charge upon lithiation at gradually increasing C-rates of the FSP-made LTO (Fig. 4, squares). The data in Fig. 7a are obtained from electrodes of 2.8 mg/cm^2 loading and 10 wt% conducting CB content. The data in Fig.7b are obtained from thinner electrodes of 1.5 mg/cm^2 loading and higher CB content of 15 wt%.

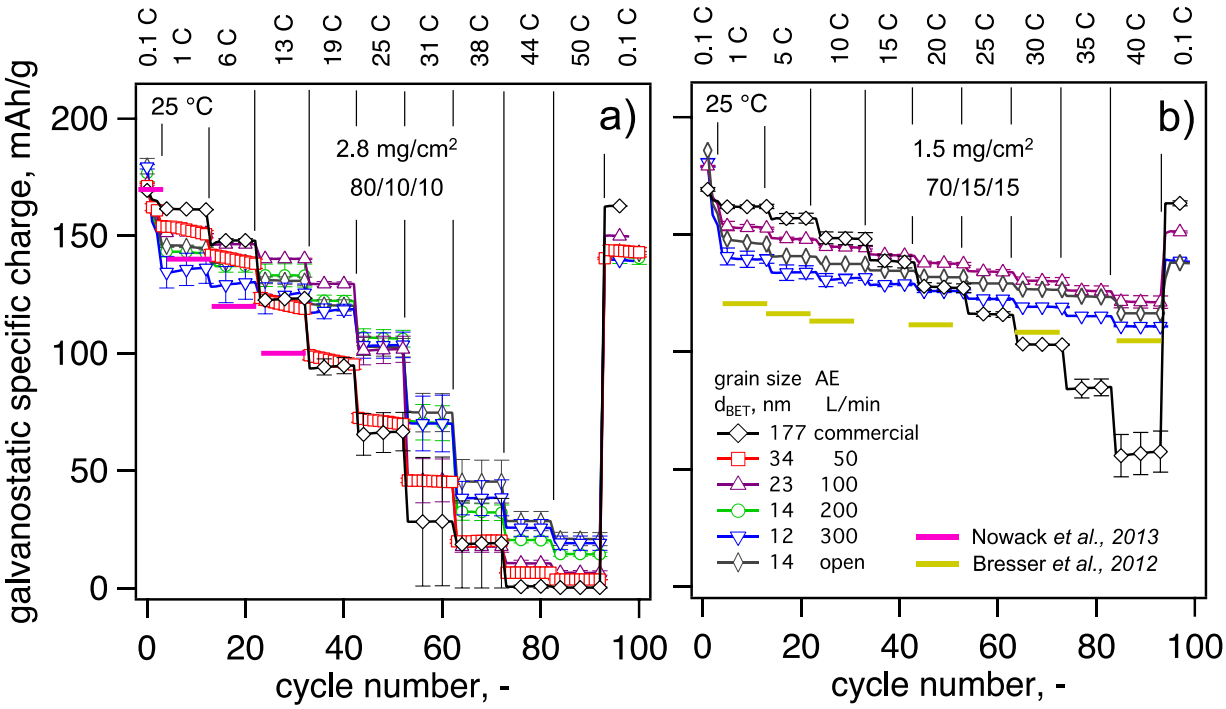

Fig. 7. Galvanostatic specific charge upon lithiation at various C-rates of electrodes made from as-synthesized LTO nanoparticles in comparison to commercial battery grade LTO. Superior high-C-rate electrochemical performance is obtained for the smallest FSP-made particles of d_{BET}= 12 to 14 where the larger ones of d_{BET} =23 and 34 nm as well as commercial LTO of d_{BET} = 177 nm shows relatively lower specific charge at high C-rates

For comparison, relatively large commercial LTO (d_{BET} = 177 nm) was processed and tested similarly (diamonds). The high but irreversible specific charge of small LTO during initial lithiation (Fig. 6) is seen also here, followed by a rapid charge decay within the first 3-4 cycles. This effect, however, is not seen for the relatively large (177 nm) commercial LTO particles that provide near theoretical specific charge of about 170 mAh/g.

Also in the subsequent cycles at low C-rates (less than 6C in Fig. 7a and 10C in Fig. 7b) the electrodes containing the largest particles (diamonds) provide the highest specific charge of 150 to 160 mAh/g where the smallest (d_{BET} = 12 nm, triangles down) deliver only 130 to 140 mAh/g for both electrode compositions. For particle sizes in between, the specific charge scales with LTO particle size as more pronounced LTO lattice defects in small particles reduce specific charge (Kavan et al., 2003). At these relatively low C-rates approximately the same performance is obtained from both electrode weight loadings and compositions for identical LTO particle size. This is expected since charge transfer resistance (diffusion limitation in electrode) and Ohmic resistance are not critical at low C-rates.

For higher C-rates (above 13C in Fig. 7a and 25C in Fig. 7b), however, the smaller particles of d_{BET} = 23 (triangles up), 14 (open & filled circles) and 12 nm (triangles down) deliver superior specific charge compared to the larger ones of d_{BET}= 177 nm (diamonds) due to their shorter Li-diffusion path length. They also show higher performance than, for example, microwave-assisted wet-made porous LTO particles (Nowack et al., 2013) (pink lines in Fig. 7a) as well as spray-dried porous ones (Hsiao et al., 2008). Both materials consist of nanosized primary particles of about 150 and 36 nm, respectively, consolidated in micron-sized secondary particles. The high C-rate performance of FSP-made LTO presented here is also higher than that of nano LTO (Bresser et al., 2012) (d_{BET} = 19 nm) made by FSP (yellow lines in Fig. 7b) at similar electrode weight loading and identical electrode composition. This difference may be attributed to the improved purity of LTO (less TiO_2 impurity) obtained here (Fig. 5) by a scalable, single step process.

4. CONCLUSIONS

Air entrainment (*AE*) controls the product primary particle diameter during particle synthesis in scalable, tube-enclosed FSP. Here the underlying phenomena to this size-tuning operation are elucidated by computational fluid dynamics (CFD). At low *AE*, the tube temperature increases by minimal dilution with entrained air prolonging and broadening the aerosol residence time distribution by recirculation. These effects lead to the typically larger primary particles made in enclosed than open FSP configurations. This versatile and low cost technique is applied for size-controlled synthesis of battery active LTO (d_{BET} = 60 - 13 nm) and LFP (d_{BET} = 55 - 12 nm) as well as ZrO_2 (d_{BET} = 30 - 15 nm) by varying *AE* (0-300 L/min) into a 20 cm long enclosing tube in good agreement with literature for CuO (d_{BET} = 45 - 10 nm). As prepared, battery-active LTO particles are crystalline and quite pure resulting in high C-rate performance with more than 120 mAh/g galvanostatic specific charge at 40C outperforming commercial LTO. Tube-enclosed FSP thus offers a fast, scalable and size-controlled method to produce the intrinsically safe LTO with superior performance at high C-rate.

The research leading to these results has received funding from the European Research Council under the European Union's Seventh Framework Program (FP7 / 2007-2013) / ERC grant agreement n° 247283. We thank Dr. F. Krumeich (ETHZ) and the Electron Microscopy Center of ETH Zurich (EMEZ) for TEM.

SYMBOLS

AE	air entrainment, L/min
D	dispersion gas flow rate, L/min
d_{BET}	Brunauer–Emmett–Teller (primary particle) diameter, nm
d_{XRD}	x-ray diffraction (crystallite) diameter, nm
F	pilot flame gas flow rate, L/min
ID	inner tube diameter, cm
L	mean beam length, cm
m_0	net mass flow, kg/s
m_p	melting point, K
m_r	recirculation mass flow, kg/s
P	precursor flow rate, mL/min
S	sheath gas flow rate, L/min
SEI	solid electrolyte interphase

Greek symbols

σ_g geometric standard deviation

τ mean residence time, ms

REFERENCES

Armand M., Tarascon J.M., 2008. Building better batteries. *Nature*, 451, 652-657. DOI: 10.1038/451652a.

Asbrink S., Norrby L.J., 1970. A refinement of crystal structure of copper(2) oxide with a discussion of some exceptional E.s.d.'s. *Acta Crystall. B-Stru.*, B 26, 8-15. DOI: 10.1107/S0567740870001838.

Athanassiou E.K., Grass R.N., Stark W.J., 2006. Large-scale production of carbon-coated copper nanoparticles for sensor applications. *Nanotechnology*, 17, 1668-1673. DOI: 10.1088/0957-4484/17/6/022.

Birozzi A., Copley M., von Zamory J., Pasqualini M., Calcaterra S., Nobili F., Di Cicco A. Rajantie H., Briceno M., Bilbé E., Cabo-Fernandez L., Hardwick L.J., Bresser D. Passerini St., 2015. Scaling up "nano" $Li_4Ti_5O_{12}$ for high-power lithium-ion anodes using large flame spray pyrolysis. *J. Electrochem. Soc.*, 162, A2331-A2338. DOI: 10.1149/2.0711512jes.

Bresser D., Paillard E., Copley M., Bishop P., Winter M., Passerini S., 2012. The importance of "going nano" for high power battery materials. *J. Power Sources*, 219, 217-222. DOI: 10.1016/J.Jpowsour.2012.07.035.

Curtet R., 1958. Confined jets and recirculation phenomena with cold air. *Combust Flame*, 2, 383-411. DOI: 10.1016/0010-2180(58)90032-4.

Deschanvres A., Raveau B., Sekkal Z., 1971. Synthesis and crystallographic study of new solid solution of spinelle $Li_{1+x}Ti_{2-x}O_4$ less than or equal to x less than or equal to 0,333. *Mater. Res. Bull.*, 6, 699-704. DOI: 10.1016/0025-5408(71)90103-6.

Du Pasquier A., Huang C.C., Spitler T., 2009. Nano $Li_4Ti_5O_{12}$-$LiMn_2O_4$ batteries with high power capability and improved cycle-life. *J. Power Sources*, 186, 508-514. DOI: 10.1016/J.Jpowsour.2008.10.018.

Ernst F.O., Kammler H.K., Roessler A., Pratsinis S.E., Stark W.J., Ufheil J., Novák P., 2007. Electrochemically active flame-made nanosized spinels: $LiMn_2O_4$, $Li_4Ti_5O_{12}$ and $LiFe_5O_8$. *Mater. Chem. Phys.*, 101, 372-378. DOI: 10.1016/j.matchemphys.2006.06.014.

Ferg E., Gummow R.J., de Kock A., Thackeray M.M., 1994. Spinel anodes for lithium-ion batteries. *J. Elchem Soc.*, 141, L147-L150. DOI: 10.1149/1.2059324.

Gaberscek M., Dominko R., Jamnik J., 2007. Is small particle size more important than carbon coating? An example study on $LiFePO_4$ cathodes. *Electrochem. Commun.*, 9, 2778-2783. DOI: 10.1016/J.Elecom.2007.09.020.

Gamba I.L., Damian S.M., Estenoz D.A., Nigro N., Storti M.A., Knoeppel D., 2012. Residence time distribution determination of a continuous stirred tank reactor using computational fluid dynamics and its application on the mathematical modeling of styrene polymerization. *Int. J. Chem. React. Eng.*, 10, 1-32. DOI: 10.1515/1542-6580.3057.

Groehn A.J., Pratsinis S.E., Sanchez-Ferrer A., Mezzenga R., Wegner K., 2014. Scale-up of nanoparticle synthesis by flame spray pyrolysis: The high-temperature particle residence time. *Ind. Eng. Chem. Res.*, 53, 10734-10742. DOI: 10.1021/Ie501709s.

Groehn A.J., Pratsinis S.E., Wegner K., 2012. Fluid-particle dynamics during combustion spray aerosol synthesis of ZrO_2. *Chem. Eng. J.*, 191, 491-502. DOI: 10.1016/J.Cej.2012.02.093.

He Y.B., Li B., Liu M., Zhang C., Lv W., Yang C., Li J., Du H., Zhang B., Yang Q.H., Kim J.K., Kang F., 2012. Gassing in $Li_4Ti_5O_{12}$-based batteries and its remedy. *Scientific Reports*, 2, 1-9. DOI: 10.1038/srep00913.

Hsiao K.C., Liao S.C., Chen J.M., 2008. Microstructure effect on the electrochemical property of $Li_4Ti_5O_{12}$ as an anode material for lithium-ion batteries. *Electrochim. Acta*, 53, 7242-7247. DOI: 10.1016/J.Electacta.2008.05.002.

Hudak N.S., Huber D.L., 2012. Size effects in the electrochemical alloying and cycling of electrodeposited aluminum with lithium. *J. Electrochem. Soc.*, 159, A688-A695. DOI: 10.1149/2.023206jes.

Jiang J.W., Chen J., Dahn J.R., 2004. Comparison of the reactions between $Li_{7/3}Ti_{5/3}O_4$ or LiC_6 and nonaqueous solvents or electrolytes using accelerating rate calorimetry. *J. Electrochem. Soc.*, 151, A2082-A2087. DOI: 10.1149/1.1817698.

Johannessen T., Pratsinis S.E., Livbjerg H., 2000. Computational fluid-particle dynamics for the flame synthesis of alumina particles. *Chem. Eng. Sci.*, 55, 177-191. DOI: 10.1016/S0009-2509(99)00183-9.

Karhunen T., Lähde A., Leskinen J., Büchel R., Waser O., Tapper U., Jokiniemi J., 2011. Transition metal-doped lithium titanium oxide nanoparticles made using flame spray pyrolysis. *ISRN Nanotechnology*, 2011, 1-6. DOI: 10.5402/2011/180821.

Kavan L., Prochazka J., Spitler T.M., Kalbac M., Zukalova M.T., Drezen T., Gratzel M., 2003. Li insertion into $Li_4Ti_5O_{12}$ (Spinel) - Charge capability vs. particle size in thin-film electrodes. *J. Electrochem. Soc.*, 150, A1000-A1007. DOI: 10.1149/1.1581262.

Kho Y.K., Teoh W.Y., Madler L., Amal R., 2011. Dopant-free, polymorphic design of TiO_2 nanocrystals by flame aerosol synthesis. *Chem. Eng. Sci.*, 66, 2409-2416. DOI: 10.1016/J.Ces.2011.02.058.

Krumeich F., Waser O., Pratsinis S.E. 2016. Thermal annealing dynamics of carbon-coated $LiFePO_4$ nanoparticles studied by in-situ analysis. *J. Solid State Chem.* 242, 96-102. DOI: 10.1016/j.jssc.2016.07.002

Laruelle S., Grugeon S., Poizot P., Dolle M., Dupont L., Tarascon J.M., 2002. On the origin of the extra electrochemical capacity displayed by MO/Li cells at low potential. *J. Electrochem. Soc.*, 149, A627-A634. DOI: 10.1149/1.1467947.

Levenspiel O., 1999. *Chemical reaction engineering*. Wiley, New York.

Madler L., Kammler H.K., Mueller R., Pratsinis S.E., 2002. Controlled synthesis of nanostructured particles by flame spray pyrolysis. *J. Aerosol Sci.*, 33, 369-389. DOI: 10.1016/S0021-8502(01)00159-8.

Madler L., Stark W.J., Pratsinis S.E., 2002. Flame-made ceria nanoparticles. *J. Mater. Res.*, 17, 1356-1362. DOI: 10.1557/jmr.2002.0202.

Magnussen B.F., Hjertager B.H., 1977. On mathematical modeling of turbulent combustion with special emphasis on soot formation and combustion. *Symp. Int. Combust.*, 16, 719-729. DOI: 10.1016/S0082-0784(77)80366-4.

Morrison P.W., Raghavan R., Timpone A.J., Artelt C.P., Pratsinis S.E., 1997. In situ Fourier transform infrared characterization of the effect of electrical fields on the flame synthesis of TiO_2 particles. *Chem. Mater.*, 9, 2702-2708. DOI: 10.1021/cm960508u.

Mueller R., Kammler H.K., Pratsinis S.E., Vital A., Beaucage G., Burtscher P., 2004. Non-agglomerated dry silica nanoparticles. *Powder Technol.*, 140, 40-48. DOI: 10.1016/J.Powtec.2004.01.004\.

Mueller R., Madler L., Pratsinis S.E., 2003. Nanoparticle synthesis at high production rates by flame spray pyrolysis. *Chem. Eng. Sci.*, 58, 1969-1976. DOI: 10.1016/s0009-2509(03)00022-8

Naoi K., Naoi W., Aoyagi S., Miyamoto J., Kamino T., 2013. New generation "nanohybrid supercapacitor". *Accounts Chem. Res.*, 46, 1075-1083. DOI: 10.1021/Ar200308h.

Nowack L.V., Waser O., Yarema O., Wood V., 2013. Rapid, microwave-assisted synthesis of battery-grade lithium titanate (LTO). *RSC Adv.*, 3, 15618-15621. DOI: 10.1039/C3ra43237h.

Ohzuku T., Ueda A., Yamamoto N., 1995. Zero-strain insertion material of $Li[Li_{1/3}ti_{5/3}]O_4$ for rechargeable lithium cells. *J. Electrochem. Soc.*, 142, 1431-1435. DOI: 10.1149/1.2048592.

Olfe D.B., 1961. Mean beam length calculations for radiation from non-transparent gases. *J. Quant. Spectrosc. Ra.*, 1, 169-176. DOI: 10.1016/0022-4073(61)90022-X.

Padhi A.K., Nanjundaswamy K.S., Goodenough J.B. (1997). Phospho-olivines as positive-electrode materials for rechargeable lithium batteries. *J. Electrochem. Soc.,* 144, 1188-1194. DOI: 10.1149/1.1837571

Poullikkas A., 2013. A comparative overview of large-scale battery systems for electricity storage. *Renew. Sust. Energ. Rev.*, 27, 778-788. DOI: 10.1016/J.Rser.2013.07.017.

Pratsinis S.E., 1998. Flame aerosol synthesis of ceramic powders. *Prog. Energ. Combust.*, 24, 197-219. DOI: 10.1016/S0360-1285(97)00028-2.

Rudin T., Wegner K., Pratsinis S.E., 2011. Uniform nanoparticles by flame-assisted spray pyrolysis (FASP) of low cost precursors. *J. Nanopart. Res.*, 13, 2715-2725. DOI: 10.1007/s11051-010-0206-x.

Sotiriou G.A., Sannomiya T., Teleki A., Krumeich F., Voros J., Pratsinis S.E., 2010. Non-toxic dry-coated nanosilver for plasmonic biosensors. *Adv. Funct. Mater.*, 20, 4250-4257. DOI: 10.1002/Adfm.201000985.

Streltsov V.A., Belokoneva E.L., Tsirelson V.G., Hansen N. K., 1993. Multipole analysis of the electron-density in triphylite, $LiFePO_4$, using X-ray-diffraction data. *Acta Crystallogr. B*, 49, 147-153. DOI: 10.1107/S0108768192004701.

Strobel R., Pratsinis S.E., 2007. Flame aerosol synthesis of smart nanostructured materials. *J. Mater. Chem.*, 17, 4743-4756. DOI: 10.1039/b711652g.

Strobel R., Pratsinis S.E., 2009. Direct synthesis of maghemite, magnetite and wustite nanoparticles by flame spray pyrolysis. *Adv. Powder Technol.*, 20, 190-194. DOI: 10.1016/j.apt.2008.08.002.

Teleki A., Heine M.C., Krumeich F., Akhtar M.K., Pratsinis S.E., 2008. In situ coating of flame-made TiO_2 particles with nanothin SiO_2 films. *Langmuir*, 24, 12553-12558. DOI: 10.1021/La801630z.

Teleki A., Pratsinis S.E., Kalyanasundaram K., Gouma P.I., 2006. Sensing of organic vapors by flame-made TiO_2 nanoparticles. *Sens. Actuator B-Chem.*, 119, 683-690. DOI: 10.1016/j.snb.2006.01.027.

Teoh W.Y., Amal R., Madler L., 2010. Flame spray pyrolysis: An enabling technology for nanoparticles design and fabrication. *Nanoscale*, 2, 1324-1347. DOI: 10.1039/C0nr00017e.

Vlad A., Singh N., Rolland J., Melinte S., Ajayan P.M., Gohy J.F., 2014. Hybrid supercapacitor-battery materials for fast electrochemical charge storage. *Sci. Rep.*, 4, 1-7. DOI: 10.1038/Srep04315.

Wagemaker M., van Eck E.R.H., Kentgens A.P.M., Mulder F.M., 2009. Li-ion diffusion in the equilibrium nanomorphology of spinel $Li_{4+x}Ti_5O_{12}$. *J. Phys. Chem. B*, 113, 224-230. DOI: 10.1021/Jp8073706.

Waser O., Buchel R., Hintennach A., Novák P., Pratsinis S.E., 2011. Continuous flame aerosol synthesis of carbon-coated nano-$LiFePO_4$ for Li-ion batteries. *J. Aerosol Sci.*, 42, 657-667. DOI: 10.1016/J.Jaerosci.2011.06.003.

Waser O., Groehn A.J., Eggersdorfer M.L., Pratsinis S.E., 2014. Air entrainment during flame aerosol synthesis of nanoparticles. *Aerosol Sci. Technol.*, 48, 1195-1206. DOI: 10.1080/02786826.2014.969800.

Waser O., Hess M., Guntner A., Novák P., Pratsinis S.E., 2013. Size controlled CuO nanoparticles for Li-ion batteries. *J. Power Sources*, 241, 415-422. DOI: 10.1016/J.Jpowsour.2013.04.147.

Wegner K., Pratsinis S.E., 2003. Scale-up of nanoparticle synthesis in diffusion flame reactors. *Chem. Eng. Sci.*, 58, 4581-4589. DOI: 10.1016/J.Ces.2003.07.010.

Wegner K., Schimmoeller B., Thiebaut B., Fernandez C., Rao T.N., 2011. Pilot plants for industrial nanoparticle production by flame spray pyrolysis. *Kona Powder Part J.*, 251-265. DOI: 10.14356/kona.2011025.

Whitney E., 1994. *Ceramic cutting tools : materials, development, and performance*. Noyes Publications, Park Ridge, New Jersey, USA.

Zheng H.H., Li J., Song X.Y., Liu G., Battaglia V.S., 2012. A comprehensive understanding of electrode thickness effects on the electrochemical performances of Li-ion battery cathodes. *Electrochim Acta*, 71, 258-265. DOI: 10.1016/J.Electacta.2012.03.161.

Received 04 October 2016
Received in revised form 18 February 2017
Accepted 20 February 2017

APPENDICES

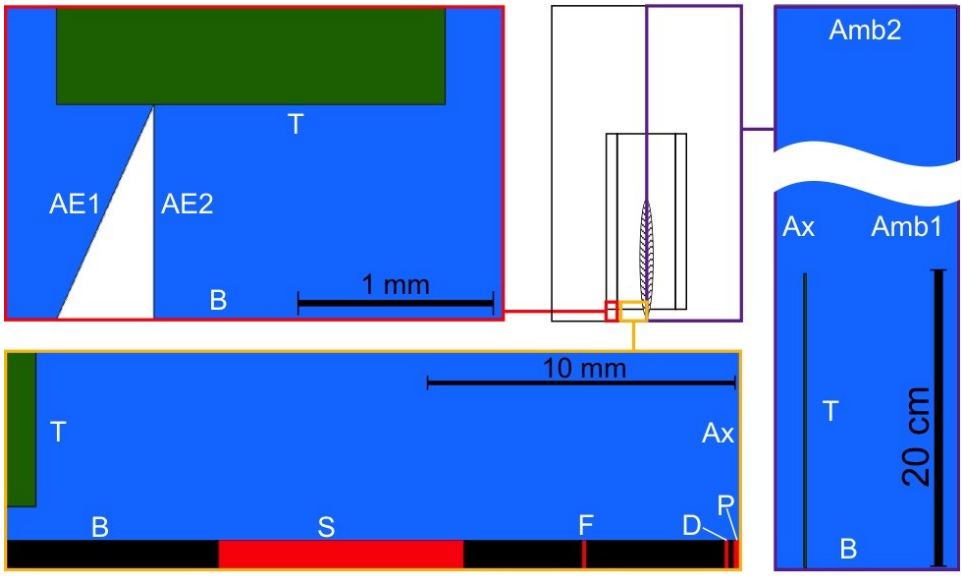

Fig. A1. Geometry of the simulation domain with fluid zone in blue and the 20 cm long tube (T) in green. The whole domain is depicted on the right (purple frame) and shows the tube on the lower left side. Total radius is 15 cm and total height is 100 cm. Top (Amb1) and right border (Amb2) have pressure boundary conditions assigned. The left edge corresponds to the symmetry axis (Ax) and the bottom end is given by the burner wall (B). The lower section (yellow frame) depicts the detailed burner geometry with red marked inlets from left to right for

sheath gas (S), pilot flame (F), dispersion gas (D) and liquid precursor (P). The green square on the left side marks the tube (T) while the right-hand border of the figure is coincident with the symmetry axis (Ax). Detailed geometry of the air entrainment boundaries is depicted in the upper left corner (red frame). Boundary conditions for *AE* inlet (AE2) and outlet (AE1) are assigned to the edges of the white triangle

Table A1. Boundary conditions for the FSP simulations. All boundaries but the tube are at 300 K (labels in brackets refer to Fig. A1).

Boundary	Type	Material (mole %.)	Comment
Burner (B)	Wall	Aluminium (-)	No slip
Tube (T)	Wall	Quartz glass (-)	No slip; temperature set by heat transfer
Axis (Ax)	Axis	-	-
Inlet-Ambient (Amb1)	Pressure-inlet	N_2 (79); O_2 (21)	Ambient pressure
Outlet-Ambient (Amb2)	Pressure-outlet	N_2 (79); O_2 (21)	Gauge pressure: -10 Pa; draft of fume hood
Inlet-*AE* (AE2)	Mass-flow-inlet	N_2 (79); O_2 (21)	Negative radial flow direction;
Outlet-*AE* (AE1)	Pressure-outlet	N_2 (79); O_2 (21)	Flow normal to boundary
Sheath (*S*)	Mass-flow-inlet	O_2 (100)	Flow normal to boundary
Pilot flame (*F*)	Mass-flow-inlet	O_2 (66.7); CH_4 (33.3)	Flow normal to boundary
Dispersion gas (*D*)	Mass-flow-inlet	O_2 (100)	Ma ≈ 1
Precursor (*P*)	Wall	C_8H_{10} (32.1); $C_8H_{16}O_2$ (67.9)	